ANZIAM J. 57(2015), 114–137
doi:10.1017/S1446181115000255

NUMERICAL STABILITY AND ACCURACY OF THE SCALED BOUNDARY FINITE ELEMENT METHOD IN ENGINEERING APPLICATIONS

MIAO LI[1,3], YONG ZHANG[2], HONG ZHANG✉[1] and HONG GUAN[1]

(Received 30 January, 2015; accepted 22 May, 2015)

Abstract

The scaled boundary finite element method (SBFEM) is a semi-analytical computational method initially developed in the 1990s. It has been widely applied in the fields of solid mechanics, oceanic, geotechnical, hydraulic, electromagnetic and acoustic engineering problems. Most of the published work on SBFEM has focused on its theoretical development and practical applications, but, so far, no explicit discussion on the numerical stability and accuracy of its solution has been systematically documented. However, for a reliable engineering application, the inherent numerical problems associated with SBFEM solution procedures require thorough analysis in terms of its causes and the corresponding remedies. This study investigates the numerical performance of SBFEM with respect to matrix manipulation techniques and their properties. Some illustrative examples are given to identify reasons for possible numerical difficulties, and corresponding solution schemes are proposed to overcome these problems.

2010 *Mathematics subject classification*: primary 65M12; secondary 65M38, 65M60, 00A73.

Keywords and phrases: SBFEM, numerical stability and accuracy, matrix decomposition, nondimensionalization, engineering application.

1. Introduction

The development of SBFEM dates back to the mid-1990s [25]. Initially, it was termed as the consistent infinitesimal finite-element cell method, and later renamed as the scaled boundary finite element method, when the concept of solving problems was better understood. Since then, SBFEM has been used in various engineering fields with

[1]Griffith School of Engineering, Griffith University, Queensland 4222, Australia;
e-mail: hong.zhang@griffith.edu.au.
[2]Institute of Nuclear Energy Safety Technology, Chinese Academy of Sciences, Hefei, Anhui 230031, China.
[3]Engineering, Faculty of Business, Charles Sturt University, Bathurst, NSW 2795, Australia.

rapid recognition and acknowledgement. Apart from the wave propagation problem within the framework of dynamic unbounded medium-structure interaction, from which the concept of SBFEM was originally derived, SBFEM has been employed in fracture mechanics [28–30] by taking advantage of its capability to accurately capture the stress intensification around the crack tips. It has also been applied to solve wave diffraction problems around breakwaters and caissons by many researchers [10, 11, 23, 24]. Subsequently, SBFEM has been reformulated in computational electromagnetics to address waveguide eigenproblems [13], extending its application to a new area.

Similar to other numerical methods, one of the most significant concerns in assessing the practical applicability of SBFEM is the reliability of its solution; more specifically, the numerical stability and accuracy of its calculations. The original partial differential equations (PDEs) governing the physical problem, through the scaled boundary coordinate transformation and the weighted residual technique, is rewritten in the matrix form of ordinary differential equations (ODEs), that is, the scaled boundary finite element equation. The term matrix refers to the coefficient matrices of the equation, which are calculated from the discretization information of the domain boundary and are in the form of matrices. These coefficient matrices are used to formulate a Hamiltonian matrix, of which a matrix decomposition is to be performed. The level of accuracy of the Hamiltonian matrix decomposition is a prerequisite for a valid SBFEM calculation. On the other hand, SBFEM is essentially vulnerable to the unavoidable rounding error associated with floating-point arithmetic, especially when the magnitudes of matrix entries calculated from input parameters differ significantly over a vast range. The rounding error can intensify over a sequence of matrix manipulations, especially matrix inversions, to such an unmanageable extent that it renders the SBFEM calculation meaningless.

Most of the literature in this area has focused on the theoretical development of SBFEM to derive its conceptual framework [6, 20–22, 26, 27] and the technical issues related to the solution algorithms of the scaled boundary finite element equation [1, 2, 12, 17, 18]. No explicit emphasis has been given to the numerical stability and accuracy of the SBFEM solution, which motivates a discussion on its practical applicability. The goal of this study is to fill in this gap in the research, that is, to explore the numerical credibility of SBFEM, detect the technical reasons for potential instability and inaccuracy and propose solution schemes to overcome these problems.

2. Basic formulation of SBFEM

The concept of SBFEM originates from two robust numerical methods, that is, the finite element method (FEM) and the boundary element method (BEM). By scaling the discretized boundary of the study domain with respect to a centre, either outwards to address an unbounded domain or inwards for a bounded domain, SBFEM describes the problem by using a radial coordinate and two circumferential coordinates. This reduces the spatial dimension of the problem by one in the solution process, as

https://doi.org/10.1017/S1446181115000255 Published online by Cambridge University Press

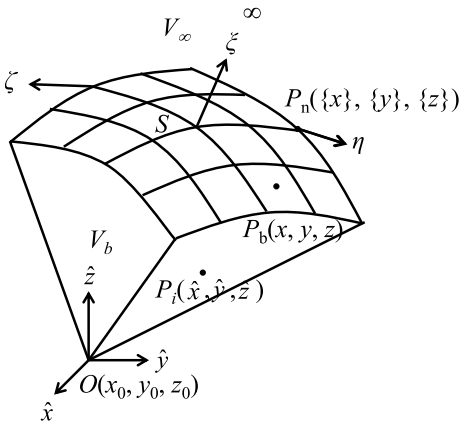

FIGURE 1. Definition of the scaled boundary coordinate system [20].

in the BEM. The discretization and assembly concepts are inherited from FEM; however, they are only applied on the boundary, which significantly minimizes the discretization effort and leads to substantially reduced degrees of freedom.

Detailed and systematic descriptions of key technical derivations of SBFEM and its solution schemes are abundantly documented, and hence will not be repeated here. However, we outline a three-dimensional illustration of a bounded elastic problem to introduce some key equations for later reference.

The scaled boundary coordinate system (ξ, η, ζ), with ξ denoting the radial coordinate and η and ζ for the circumferential coordinates, is illustrated in Figure 1. It is interrelated to the Cartesian coordinate system ($\hat{x}$, $\hat{y}$, $\hat{z}$) by the mapping function $[N(\eta, \zeta)]$ as

$$\begin{aligned} \hat{x}(\xi, \eta, \zeta) &= \xi[N(\eta, \zeta)]\{x\} + x_0, \\ \hat{y}(\xi, \eta, \zeta) &= \xi[N(\eta, \zeta)]\{y\} + y_0, \\ \hat{z}(\xi, \eta, \zeta) &= \xi[N(\eta, \zeta)]\{z\} + z_0, \end{aligned} \tag{2.1}$$

where $(\{x\}, \{y\}, \{z\})$ represents a nodal point on the discretized boundary and (x_0, y_0, z_0) represents the scaling centre O with respect to which the boundary is scaled. Note that, as a convention in SBFEM, the coordinate of the Cartesian space is represented by $(\hat{x}, \hat{y}, \hat{z})$, and (x, y, z) is reserved for the coordinates on the boundary. However, x, y and z are still used when indicating directions in the following discussions.

Equation (2.1), on which the scaled boundary transformation is based, is the core of the SBFEM concept. The governing differential equations for elasto-dynamic problems are shown in equation (2.2), with $[L]$ representing the differential operator, $\{\sigma\}$ the stress amplitude, $\{\varepsilon\}$ the strain amplitude, $\{u\}$ the displacement amplitude, $[D]$ the elastic matrix, ω the excitation frequency and ρ the mass density: that is,

$$\begin{aligned} [L]^T\{\sigma\} + \omega^2\rho\{u\} &= 0, \\ \{\sigma\} &= [D]\{\varepsilon\}, \\ \{\varepsilon\} &= [L]\{u\}. \end{aligned} \tag{2.2}$$

https://doi.org/10.1017/S1446181115000255 Published online by Cambridge University Press

Equation (2.2) is weakened along the discretized circumferential direction by using either the weighted residual technique or the variational principle. Consequently, the scaled boundary finite element equation in the nodal displacement function $\{u(\xi)\}$ yields

$$[E^0]\xi^2\{u(\xi)\}_{,\xi\xi} + (2[E^0] + [E^1]^T - [E^1])\xi\{u(\xi)\}_{,\xi} + ([E^1]^T - [E^2])\{u(\xi)\} + \omega^2[M^0]\xi^2\{u(\xi)\} = 0 \tag{2.3}$$

with the internal nodal force

$$\{q(\xi)\} = [E^0]\xi^2\{u(\xi)\}_{,\xi} + [E^1]^T\xi\{u(\xi)\}, \tag{2.4}$$

where $[E^0]$, $[E^1]$, $[E^2]$ and $[M^0]$ are the coefficient matrices obtained by boundary discretization and assemblage.

Equation (2.3) is termed as the scaled boundary finite element equation. It is a linear second-order matrix-form ODE, the solution $\{u(\xi)\}$ of which represents the analytical variation of the nodal displacement in the radial direction. For elasto-static problems with $\omega = 0$, equations (2.3) and (2.4) are formulated on the boundary where $\xi = 1$. The nodal force $\{R\}$ and nodal displacement $\{u\}$ are related by

$$\{R\} = [K]\{u\}, \tag{2.5}$$

with $[K]$ representing the static stiffness matrix on the boundary. Equation (2.3) is solved by introducing the variable $\{X(\xi)\}$ to incorporate the nodal displacement function $\{u(\xi)\}$ and the nodal force function $\{q(\xi)\}$ as

$$\{X(\xi)\} = \begin{Bmatrix} \xi^{0.5}\{u(\xi)\} \\ \xi^{-0.5}\{q(\xi)\} \end{Bmatrix}. \tag{2.6}$$

This yields the first-order ODE

$$\xi\{X(\xi)\}_{,\xi} = -[Z]\{X(\xi)\}, \tag{2.7}$$

where in terms of $[E^0]$, $[E^1]$, $[E^2]$ and the identity matrix $[I]$,

$$[Z] = \begin{bmatrix} [E^0]^{-1}[E^1]^T - 0.5(s-2)[I] & -[E^0]^{-1} \\ -[E^2] + [E^1][E^0]^{-1}[E^1]^T & -[E^1][E^0]^{-1} + 0.5(s-2)[I] \end{bmatrix},$$

with s representing the spatial dimension of the study domain ($s = 2$ or 3 for two- or three-dimensional problems, respectively). For elasto-dynamic problems, the nodal displacement function $\{u(\xi)\}$ records the displacement variation history with respect to time. The relationship of nodal force $\{R\}$ and nodal displacement $\{u\}$ is introduced as

$$\{R\} = [S(\omega)]\{u\}, \tag{2.8}$$

with $[S(\omega)]$ representing the dynamic stiffness matrix. With $\{R\} = \{q(\xi)\}$ at $\xi = 1$ on the boundary, the scaled boundary finite element equation is rewritten using $[S(\omega)]$ as

$$([S(\omega)] - [E^1])[E^0]^{-1}([S(\omega)] - [E^1]^T) - [E^2] + [S(\omega)] + \omega[S(\omega)]_{,\omega} + \omega^2[M^0] = 0. \tag{2.9}$$

https://doi.org/10.1017/S1446181115000255 Published online by Cambridge University Press

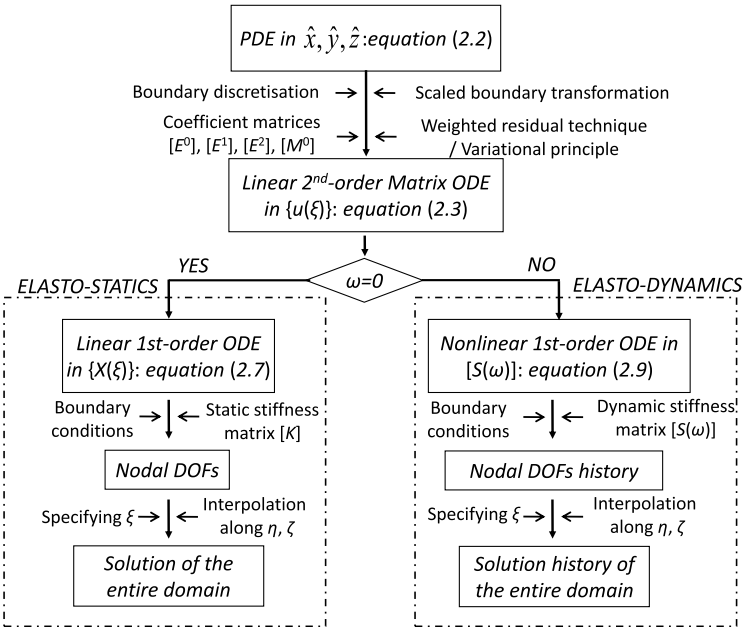

FIGURE 2. Solution procedures of SBFEM.

Equation (2.9) is a nonlinear first-order matrix-form ODE. Now the main objective is to solve the dynamic stiffness matrix $[S(\omega)]$ in equation (2.9) and substitute it back into equation (2.8) to obtain the nodal degrees of freedom $\{u\}$.

Being formulated either in $\{u(\xi)\}$ or $[S(\omega)]$, once $\{u\}$ is obtained, the solution of the entire domain can be calculated by specifying the scaled boundary coordinates ξ, η and ζ. The solution is exact in the radial direction, and it converges in the finite element sense in circumferential directions. The solution procedures described above can be illustrated by a flow chart shown in Figure 2.

3. Matrix decomposition

3.1. Eigenvalue decomposition and inherent numerical issues Some of the main techniques for solving the matrix-form scaled boundary finite element equation for both elasto-static and elasto-dynamic problems have been summarized in Section 2. A Hamiltonian matrix $[Z]$ is formulated using $[E^0]$, $[E^1]$ and $[E^2]$ of the scaled boundary finite element equation (2.3), where the nodal displacement function $\{u(\xi)\}$ is the basic unknown function. A new intermediate variable $\{X(\xi)\}$ is introduced, which reduces the second-order ODE (2.3) to a first-order ODE (2.7). By hypothesizing the displacement field in the form of the power series of the radial coordinate ξ, the solution of equation (2.7) yields

$$\{X(\xi)\} = c_1\xi^{-\lambda_1}\{\phi_1\} + c_2\xi^{-\lambda_2}\{\phi_2\} + \cdots + c_n\xi^{-\lambda_n}\{\phi_n\}, \tag{3.1}$$

https://doi.org/10.1017/S1446181115000255 Published online by Cambridge University Press

with n as the dimension of the Hamiltonian matrix $[Z]$. Substitution of equation (3.1) into equation (2.7) leads to the eigenproblem

$$[Z]\{\phi_i\} = \lambda_i\{\phi_i\} \quad \text{for } i = 1, 2, \ldots, n, \tag{3.2}$$

where λ_i is the eigenvalue of $[Z]$ and $\{\phi_i\}$ is the corresponding eigenvector. Equation (3.1) can be recast in a matrix form as

$$\{X(\xi)\} = \begin{bmatrix} [\Phi_{11}] & [\Phi_{12}] \\ [\Phi_{21}] & [\Phi_{22}] \end{bmatrix} \begin{bmatrix} [\xi^{\Lambda_1}] & \\ & [\xi^{\Lambda_2}] \end{bmatrix} \begin{Bmatrix} \{C_1\} \\ \{C_2\} \end{Bmatrix}, \tag{3.3}$$

where Λ_1 and Λ_2 are two diagonal matrices with λ_i $(i = 1, 2, \ldots, n)$ being their entries. Note that, if λ is an eigenvalue of $[Z]$, then $-\lambda$, $\bar{\lambda}$ (conjugate complex number) and $-\bar{\lambda}$ are also eigenvalues of $[Z]$. The eigenvalues λ_i of matrix $[Z]$ can be arranged in such a way that all the eigenvalues in Λ_1 have positive real parts and all the eigenvalues in Λ_2 have negative real parts. From equations (3.3) and (2.6),

$$\{u(\xi)\} = \xi^{-0.5}([\Phi_{11}][\xi^{\Lambda_1}]\{C_1\} + [\Phi_{12}][\xi^{\Lambda_2}]\{C_2\}) \tag{3.4}$$

and

$$\{q(\xi)\} = \xi^{+0.5}([\Phi_{21}][\xi^{\Lambda_1}]\{C_1\} + [\Phi_{22}][\xi^{\Lambda_2}]\{C_2\}), \tag{3.5}$$

where the integral constants $\{C_1\}$ and $\{C_2\}$ are to be determined by the given boundary conditions.

The displacement amplitude at the scaling centre, where $\xi = 0$ for a bounded domain, should be finite. Since the real parts of λ_i in Λ_2 are negative, from equations (3.4) and (3.5)

$$\{u(\xi)\} = \xi^{-0.5}[\Phi_{11}][\xi^{\Lambda_1}]\{C_1\} \tag{3.6}$$

and

$$\{q(\xi)\} = \xi^{+0.5}[\Phi_{21}][\xi^{\Lambda_1}]\{C_1\}. \tag{3.7}$$

Since $\{R\} = [K]\{u\}$ and $\{R\} = \{q(\xi = 1)\}$ on the boundary, eliminating the constant vector $\{C_1\}$ from equations (3.6) and (3.7) yields

$$[K] = [\Phi_{21}][\Phi_{11}]^{-1}. \tag{3.8}$$

Consequently, $\{u\}$ and $\{C_1\}$ can be calculated from equation (2.5) and (3.6), respectively.

After $\{C_1\}$ is determined, the nodal displacement function $\{u(\xi)\}$ along the line defined by connecting the scaling centre and the corresponding node on the boundary is analytically obtained from equation (3.6). For unbounded domains, the displacement amplitude at $\xi = \infty$ must remain finite, and $\{R\} = -\{q(\xi = 1)\}$ applies.

In real cases, however, the power series formulation may not provide a complete general solution, since logarithmic terms exist in problems involving particular geometric configurations, material composition and boundary conditions [3, 8, 15, 16]. In this case, multiple eigenvalues or near-multiple eigenvalues of the Hamiltonian matrix $[Z]$ might be present, corresponding to parallel eigenvectors and indicating the

https://doi.org/10.1017/S1446181115000255 Published online by Cambridge University Press

existence of logarithmic terms in the solution. Consequently, matrices $[\Phi_{11}]$ and $[\Phi_{21}]$ in equation (3.8) (or $[\Phi_{12}]$ and $[\Phi_{22}]$ for the case of an unbounded domain), formed by parallel eigenvectors, are rank-deficient and irreversible, which results in inaccurate solutions, or even failure of the eigenvalue decomposition when solving the scaled boundary finite element equation.

3.2. Real Schur decomposition Deeks and Wolf [5, 7] investigated a two-dimensional unbounded domain problem governed by the Laplace equation using SBFEM, in which the displacement amplitude is infinite in the nearby field. This infinite term is represented by an additional logarithmic mode, associated with the rigid body translation to the power series formulation of the solution. Song [17] proposed a matrix-function solution in combination with the real Schur decomposition to address this multiple eigenvalue issue. Terms in the series solution are not restricted to power function form. Unlike the work presented in Deeks and Wolf [5, 7], Song's [17] matrix function method does not require any prior knowledge of the presence of logarithmic terms, and copes well with the power and logarithmic functions and their transitions in the solution. Li et al. [12] further discussed the outperformance of the real Schur decomposition compared with the conventional eigenvalue decomposition technique.

The real Schur decomposition of the Hamiltonian matrix $[Z]$ can be expressed as

$$[Z] = [V][S][V]^T, \tag{3.9}$$

where $[V]$ is an orthogonal matrix and $[S]$ is a block upper triangular matrix with one-by-one and two-by-two blocks on the diagonal. The eigenvalues are revealed by the diagonal elements and the blocks of $[S]$. The columns of $[V]$ constitute a basis offering superior numerical properties to a set of eigenvectors $\{\phi_i\}$ in equation (3.2) [14]. The matrices $[S]$ and $[V]$ are partitioned into submatrices of equal size as

$$[S] = \begin{bmatrix} [S_n] & * \\ 0 & [S_p] \end{bmatrix} \quad \text{and} \quad [V] = \begin{bmatrix} [V_{u1}] & [V_{u2}] \\ [V_{q1}] & [V_{q2}] \end{bmatrix},$$

with $*$ representing a real matrix. The diagonal elements of the matrix $[S_n]$ are negative, and those of the matrix $[S_p]$ are positive. Block-diagonalizing $[S]$, using an upper-triangular matrix and equation (3.9) yields

$$[\Psi]^{-1}[Z][\Psi] = \begin{bmatrix} [S_n] & 0 \\ 0 & [S_p] \end{bmatrix}.$$

Similar to equation (3.3), the general solution of equation (2.7) using the real Schur decomposition is

$$\{X(\xi)\} = \begin{bmatrix} [\Psi_{u1}] & [\Psi_{u2}] \\ [\Psi_{q1}] & [\Psi_{q2}] \end{bmatrix} \begin{bmatrix} \xi^{-[S_n]} & \\ & \xi^{-[S_p]} \end{bmatrix} \begin{Bmatrix} \{C_1\} \\ \{C_2\} \end{Bmatrix}.$$

Accordingly,

$$\{u(\xi)\} = \xi^{-0.5}([\Psi_{u1}]\xi^{-[S_n]}\{C_1\} + [\Psi_{u2}]\xi^{-[S_p]}\{C_2\}),$$
$$\{q(\xi)\} = \xi^{+0.5}([\Psi_{q1}]\xi^{-[S_n]}\{C_1\} + [\Psi_{q2}]\xi^{-[S_p]}\{C_2\}).$$

https://doi.org/10.1017/S1446181115000255 Published online by Cambridge University Press

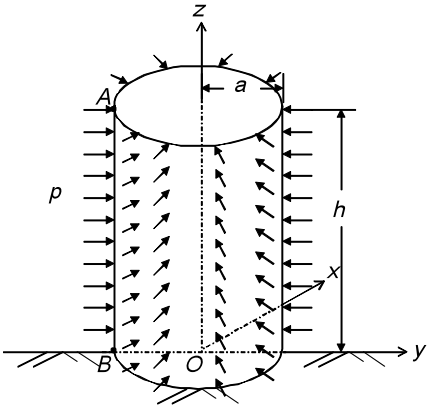

FIGURE 3. A cylindrical pile subjected to a uniformly distributed pressure.

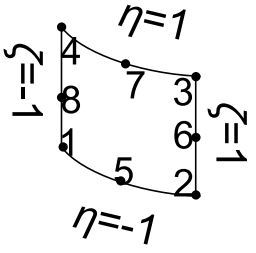

$$N_1(\eta,\zeta)=-\frac{1}{4}(\eta-1)(\zeta-1)(\eta+\zeta+1) \qquad N_2(\eta,\zeta)=\frac{1}{2}(\eta^2-1)(\zeta-1)$$

$$N_3(\eta,\zeta)=\frac{1}{4}(\zeta-1)(-\eta^2+\zeta\eta+\zeta+1) \qquad N_4(\eta,\zeta)=-\frac{1}{2}(\eta+1)(\zeta^2-1)$$

$$N_5(\eta,\zeta)=\frac{1}{4}(\eta+1)(\zeta+1)(\eta+\zeta-1) \qquad N_6(\eta,\zeta)=-\frac{1}{2}(\eta^2-1)(\zeta+1)$$

$$N_7(\eta,\zeta)=\frac{1}{4}(\eta-1)(\zeta+1)(\eta-\zeta+1) \qquad N_8(\eta,\zeta)=\frac{1}{2}(\eta-1)(\zeta^2-1)$$

FIGURE 4. A typical scaled boundary element and the shape functions.

The following solution procedure is the same as described for the eigenvalue decomposition in Section 3.1. By performing the real Schur decomposition, the inverse of a possibly close-to-singular matrix $[\Phi_{11}]$ (or $[\Phi_{12}]$) can be avoided by inverting only an upper-triangular matrix $[\Psi_{u1}]$ (or $[\Psi_{u2}]$). In addition, real Schur decomposition is more stable and suffers less from numerical difficulties than the eigenvalue decomposition. A case study is provided in the next section to demonstrate the efficiency of the real Schur decomposition.

3.3. Numerical example A cylindrical pile with radius $a = 1$ m and height $h = 10$ m, subject to uniformly distributed pressure $p = 3 \times 10^8$ Pa is shown in Figure 3. The pile at the bottom of the cylinder is fixed, and it is assumed to exhibit elastic behaviour with Young's modulus E and Poisson's ratio ν being 2.8×10^{10} Pa and 0.25, respectively. The scaling centre is chosen at the bottom centre of the pile. The circumferential boundary, as well as the top surface of the cylinder, is discretized with quadratic eight-node quadrilateral isoparametric elements. A representative scaled boundary element is shown in Figure 4, accompanied by corresponding shape function expressions. An example of the discretization scheme is illustrated in Figure 5(a).

https://doi.org/10.1017/S1446181115000255 Published online by Cambridge University Press

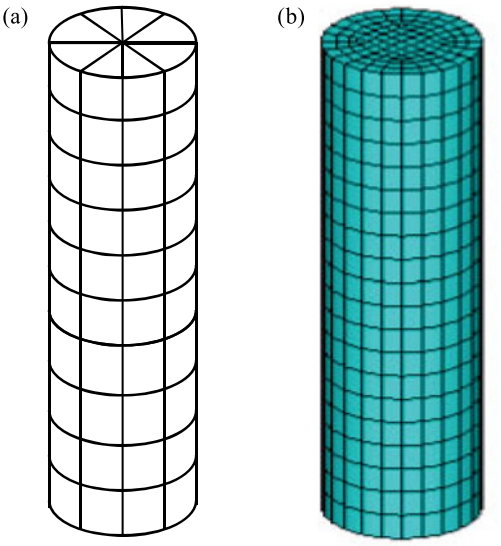

FIGURE 5. Discretization illustration of the pile foundation for (a) SBFEM model and (b) FEM model.

The real Schur decomposition is employed in the calculation. The convergence test shows that eight elements around the pile circumference are needed, one element along the radius and sixteen elements along the height of the pile. The displacement of point A (see Figure 3) on the edge of the pile head converges to 8.0357 and 52.344 mm in the x- and z-direction, respectively. In this example, a nondimensionalized SBFEM model is used to exclude the possibility of numerical inaccuracy caused by unfavourable matrix properties, such as ill-conditioning. The SBFEM nondimensionalization will be detailed in Section 4.

An equivalent FEM analysis is carried out for comparison purposes. Three-dimensional 20-node hexahedral solid elements are used in the FEM model, as shown in Figure 5(b). A convergence test shows 28 elements around the circumference, 5 elements along the radius and 50 elements for the height. The displacement of point A in the x-direction converges to 8.0357 mm, and reaches 52.345 mm in the z-direction.

The displacement profiles of line AB (see Figure 3) from both SBFEM and FEM models are plotted in Figure 6, in which lines are used to represent FEM results and markers for SBFEM results. The comparison shows excellent performance of the real Schur decomposition in the SBFEM solution process.

In order to demonstrate the superiority of the real Schur decomposition over the eigenvalue decomposition, the radial and vertical displacements of point A, calculated using the two matrix decomposition algorithms, are compared in Figure 7. The labels on the horizontal axis represent different discretization schemes. For example, $6 \times 10 \times 1$ signifies that the numbers of elements in the circumferential, vertical and radial directions are 6, 10 and 1, respectively. Unlike the eigenvalue decomposition, in

https://doi.org/10.1017/S1446181115000255 Published online by Cambridge University Press

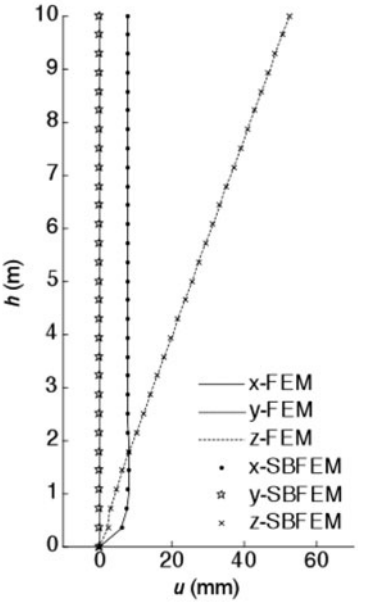

FIGURE 6. Displacement comparison between SBFEM and FEM model.

real Schur decomposition no prior knowledge of the potential multiple eigenvalues is required, and no complex number operation is performed. Moreover, the inversion of rank-deficient matrices can be efficiently avoided, and it gives more stable and reliable results compared to the eigenvalue decomposition, as shown in Figure 7.

4. SBFEM nondimensionalization

4.1. Numerical issues associated with matrix properties A cylindrical pile subject to uniformly distributed pressure, as illustrated in Figure 3, is used in this section to investigate the numerical credibility of the SBFEM calculation in relation to matrix properties. We examine the displacement components of the point A in the x-, y- and z-directions.

In the SBFEM model, the scaling centre O is chosen at the geometric centre of the pile at (0, 0, 5), and the entire surface is discretized into 184 eight-node quadratic quadrilateral elements. The solution procedure using the real Schur decomposition presented in Section 3.2 is followed. Using the raw parameters of the cylindrical pile given in Section 3.3, the displacement components in the x-, y- and z-directions of the point A are calculated as 4.431×10^3 mm, 1.421×10^4 mm and 7.178×10^4 mm, respectively. Apparently, these results differ considerably from the solutions depicted in Figure 7, which are 8.036 mm, 0 and 52.382 mm, respectively.

A close examination of the Hamiltonian matrix $[Z]$ reveals its condition number $\kappa = 2 \times 10^{24}$. This implies that the Hamiltonian matrix is ill-conditioned, and any

https://doi.org/10.1017/S1446181115000255 Published online by Cambridge University Press

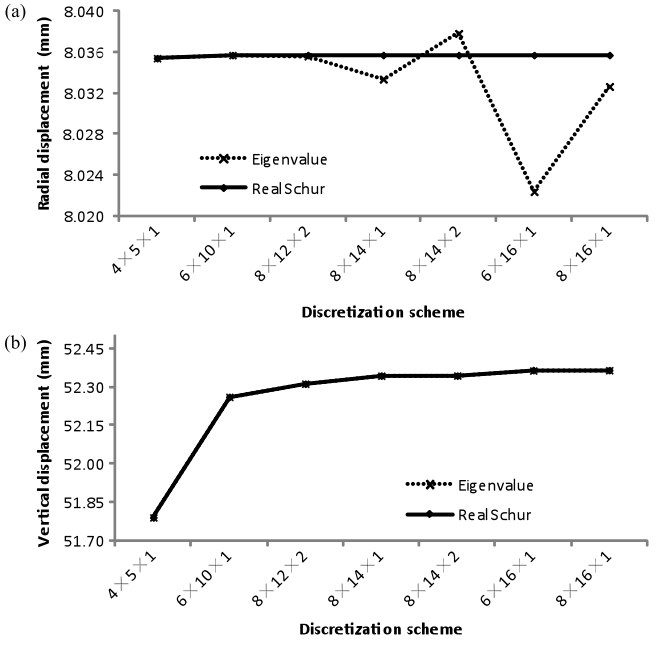

FIGURE 7. Comparison between the eigenvalue decomposition and the real Schur decomposition methods for: (a) radial displacement and (b) vertical displacement. (Note that the vertical displacements from the two methods overlap in the plot.)

subsequent manipulations either directly or indirectly related to this matrix may fail due to any rounding error fluctuation. The exactness of equation (3.9) is checked by examining the norm of a residual matrix

$$[\mathrm{Res}_1] = [Z] - [V][S][V]^T. \tag{4.1}$$

Theoretically, a norm $[Res_1] = 0$ calculated from equation (4.1) is expected. However, we obtained a norm 0.1345, which is far beyond the acceptable accuracy tolerance with an order of 10^{-7} [9].

Another examination can be associated with the static stiffness matrix $[K]$. The static stiffness matrix $[K]$, obtained from equation (3.8), should satisfy equation (2.9), with $[S(\omega)]$ and ω being replaced by $[K]$ and 0, respectively. Therefore, another residual matrix $[\mathrm{Res}_2]$ is defined in equation (4.2), which has norm 9×10^{21}: that is,

$$[Res_2] = ([K] - [E^1])[E^0]^{-1}([K] - [E^1]^T) - [E^2] + [K]. \tag{4.2}$$

By examining the Hamiltonian matrix, we find that the maximum magnitude of its entries is 10^{10}, resulting from the input parameter, that is, Young's modulus, which has a magnitude of 10^8 in the present case. The minimum magnitude, however, is zero. This significant difference in magnitudes of the matrix entries leads to the ill-conditioning of the matrix.

https://doi.org/10.1017/S1446181115000255 Published online by Cambridge University Press

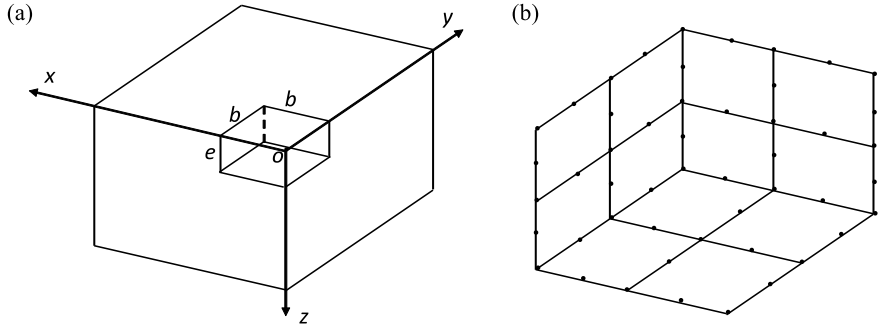

FIGURE 8. A quarter of a square prism footing embedded in a semi-infinite space: (a) the geometric plot (b) scaled boundary discretisation of the prism-medium interface.

An elastic wave propagation problem in an unbounded domain serves as another example illustrating the detrimental effects of large magnitudes of input parameters to SBFEM calculations. The case of a quarter of a square prism footing embedded in a semi-infinite half-space, as presented by Song and Wolf [19], is used herein to illustrate the problem. The geometry of the footing is reproduced in Figure 8(a) with $b = 1$ m and $e = 2/3$ m. The material properties of the half-space are assigned as follows: the shear modulus $G = 1 \times 10^{10}$ Pa, Poisson's ratio ν is $1/3$ and the mass density ρ is 2500 kg m^{-3}.

A SBFEM model is established with the scaling centre located at point O in Figure 8(a). The interface between the footing and the unbounded domain is discretized into 12 eight-node quadratic quadrilateral elements, resulting in a total of 49 nodes, as shown in Figure 8(b). The continued-fraction technique is used to formulate the dynamic stiffness matrix $[S^{\infty}(\omega)]$ in equation (2.8). Details of the continued-fraction formulation of $[S^{\infty}(\omega)]$ for an unbounded domain has been given by Bazyar and Song [1], with key equations presented below. The dynamic stiffness matrix $[S^{\infty}(\omega)]$ is decomposed as

$$[S^{\infty}(\omega)] = i\omega[C_{\infty}] + [K_{\infty}] - [Y^{(1)}(\omega)]^{-1}, \tag{4.3}$$

where $[C_{\infty}]$ and $[K_{\infty}]$ are the constant dashpot matrix and stiffness matrix, respectively. At high frequency, $[Y^{(i)}(\omega)]$ is the residual of the two-term expansion of $[S^{\infty}(\omega)]$, and in a recursive form

$$[Y^{(i)}(\omega)] = i\omega[Y_1^{(i)}] + [Y_0^{(i)}] - [Y^{(i+1)}(\omega)]^{-1} \quad (i = 1, 2, 3 \ldots),$$

where $[Y_1^{(i)}]$ and $[Y_0^{(i)}]$ are the auxiliary matrices, and the superscript i denotes the order of the continued-fraction formulation. Substituting equation (4.3) into equation (2.8) yields

$$\begin{cases} \{R(\omega)\} = (i\omega[C_{\infty}]+[K_{\infty}])\{u(\omega)\} - \{u^{(1)}(\omega)\} \\ \{u(\omega)\} = [Y^{(1)}(\omega)]\{u^{(1)}(\omega)\} \end{cases} \quad if\ i = 1$$
$$\begin{cases} \{u^{(i-1)}(\omega)\} = (i\omega[Y_1^{(i)}] + [Y_0^{(i)}])\{u^{(i)}(\omega)\} - \{u^{(i+1)}(\omega)\} \\ \{u^{(i)}(\omega)\} = [Y^{(i+1)}(\omega)]\{u^{(i+1)}(\omega)\} \end{cases} \quad if\ i > 1 \tag{4.4}$$

https://doi.org/10.1017/S1446181115000255 Published online by Cambridge University Press

and in a matrix form this can be expressed as

$$([A] + i\omega[B])\{\hat{u}(\omega)\} = \{\hat{F}(\omega)\}, \tag{4.5}$$

where $\{\hat{u}(\omega)\}$ and $\{\hat{F}(\omega)\}$ represent the displacement and external force vectors, respectively. The coefficient matrices $[A]$ and $[B]$ are formed using $[Y_1^{(i)}]$ and $[Y_0^{(i)}]$, $(i = 1, 2, 3\ldots)$ as

$$[A] = \begin{bmatrix} [K_\infty] & -[I] & & \cdots & & \\ -[I] & [Y_0^{(1)}] & -[I] & \cdots & & \\ & -[I] & [Y_0^{(2)}] & \cdots & & \\ \vdots & \vdots & \vdots & \ddots & -[I] & \\ & & & -[I] & [Y_0^{(M_{cf}-1)}] & -[I] \\ & & & & -[I] & [Y_0^{(M_{cf})}] \end{bmatrix},$$
$$[B] = \mathrm{diag}([C_\infty], [Y_1^{(1)}], [Y_1^{(2)}], \ldots, [Y_1^{(M_{cf}-1)}], [Y_1^{(M_{cf})}]). \tag{4.6}$$

The matrices $[Y_1^{(i)}]$ and $[Y_0^{(i)}]$ $(i = 1, 2, 3\ldots)$ are obtained through a series of matrices formed by using parameters such as the material density and Young's modulus (details can be found in [1]). These calculations include solving Sylvester equations and matrix inversions. Hence, the properties of the matrices involved are of significant importance to the stability and accuracy of the overall SBFEM calculations. For example, in equation (4.6), $[K_\infty]$ and $[Y_0^{(1)}]$ represent the stiffness and flexibility of the domain, respectively. The magnitude of matrix entries in $[K_\infty]$ is reciprocal to, and significantly differs from that in $[Y_0^{(1)}]$. This is analogous between $[Y_0^{(1)}]$ and $[Y_0^{(2)}], \ldots, [Y_0^{(M_{cf}-1)}]$ and $[Y_0^{(M_{cf})}]$, as shown in Table 3. Note that instead of examining any particular element in the matrix, an algebraic sum of elements corresponding to x-, y- and z-directions is performed. In the meantime, the degree of the difference amplifies as the order of the continued-fraction increases. Subsequently, upon formulating the coefficient matrix $[A]$ (analogously, matrix $[B]$) when solving equation (4.5), the difference in matrix entries of $[K_\infty]$, $[Y_0^{(1)}]$, $[Y_0^{(2)}], \ldots,$ and $[Y_0^{(M_{cf})}]$ results in the ill-conditioning of matrix $[A]$ (and $[B]$); this leads to the failure of the SBFEM solution.

From the above discussions, it is clear that input parameters should be processed prior to calculations to improve the quality of matrices for subsequent computations. This motivates the introduction of a nondimensionalization scheme into the SBFEM calculation, since it allows all quantities to have a relatively similar order of magnitude. The detailed procedure of nondimensionalization and its incorporation into the SBFEM formulation are presented in the next subsection.

https://doi.org/10.1017/S1446181115000255 Published online by Cambridge University Press

4.2. SBFEM nondimensionalization procedure Wolf and Song [25] presented a dimensional analysis, identifying independent variables related to the dynamic stiffness matrix. The nondimensionalization scheme proposed in this study follows their idea. The dimensionless length r^*, Young's modulus E^* and the mass density ρ^* are calculated using corresponding reference variables $r^* = r/r_r$, $E^* = E/E_r$ and $\rho^* = \rho/\rho_r$, respectively. The dimensions of the dynamic stiffness matrix $[S(\omega)]$ and the independent variable frequency ω are $L^{s-3}MT^{-2}$ and T^{-1}, respectively, with s representing the spatial dimension of the study domain ($s = 2$ and $s = 3$ for two- and three-dimensional problems, respectively). An equation expressing the dimensions of $[S]^{n_1} r_r^{n_2} E_r^{n_3} \rho_r^{n_4} \omega^{n_5}$ as $L^{(s-3)n_1+n_2-n_3-3n_4} M^{n_1+n_3+n_4} T^{-2n_1-2n_3-n_5}$ is used to calculate $[S^*(\omega)]$ and ω^*. Note that this equation is formed using the reference variables, rather than the corresponding material parameters, as is the case illustrated by Wolf and Song [25]. This allows more flexibility in the nondimensionalization process and yields

$$\begin{aligned}(s-3)n_1 + n_2 - n_3 - 3n_4 &= 0,\\ n_1 + n_3 + n_4 &= 0,\\ -2n_1 - 2n_3 - n_5 &= 0.\end{aligned}$$

These equations, two of which can be arbitrarily chosen, are used to determine the five parameters n_i ($i = 1, 2, 3, 4$ and 5). Given $n_1 = 1$ and $n_5 = 0$, they yield the dimensionless dynamic stiffness matrix

$$[S^*(\omega)] = r_r^{2-s} E_r^{-1} [S(\omega)], \tag{4.7}$$

or, if $n_1 = 0$ and $n_5 = 1$,

$$\omega^* = \frac{\omega r_r}{\sqrt{E_r/\rho_r}}. \tag{4.8}$$

Similarly, for the static stiffness matrix $[K]$, mass matrix $[M]$ and damping matrix $[C]$,

$$[K^*] = E_r^{-1} r_r^{-1} [K], \quad [M^*] = \rho_r^{-1} r_r^{-3} [M], \quad [C^*] = \frac{\sqrt{E_r/\rho_r}}{E_r r_r^2} [C], \tag{4.9}$$

and the coefficient matrices $[E^0]$, $[E^1]$, $[E^2]$ and $[M^0]$ are nondimensionalized as

$$\begin{aligned}[E^{0^*}] &= E_r^{-1} r_r^{2-s} [E^0], \quad [E^{1^*}] = E_r^{-1} r_r^{2-s} [E^1],\\ [E^{2^*}] &= E_r^{-1} r_r^{2-s} [E^2], \quad [M^{0^*}] = \rho_r^{-1} r_r^{-s} [M^0].\end{aligned} \tag{4.10}$$

Also, the independent variable t^* needs to be recalculated in the time-domain analysis as

$$t^* = \frac{\sqrt{E_r/\rho_r}}{r_r} t. \tag{4.11}$$

With all these above expressions, equation (2.3) retains its original form exactly. For the sake of presentation, all asterisks are removed from the mathematical expressions hereafter, unless otherwise specified.

https://doi.org/10.1017/S1446181115000255 Published online by Cambridge University Press

Corresponding to the continued-fraction formulation of the dynamic stiffness matrix $[S^{\infty}(\omega)]$ in equation (4.3), the nondimensionalized form of the relevant matrices are

$$\begin{aligned}
[C^{*}_{\infty}] &= \frac{\sqrt{E_r/\rho_r}}{E_r r_r^{s-1}}[C_{\infty}], \\
[K^{*}_{\infty}] &= E_r^{-1} r_r^{2-s}[K_{\infty}], \\
[Y_0^{(i)*}] &= (E_r r_r^{s-2})^{-N_i}[Y_0^{(i)}], \\
[Y_1^{(i)*}] &= (E_r^{0.5}\rho_r^{0.5} r_r^{s-1})^{-N_i}[Y_1^{(i)}] \quad (N_i = (-1)^i).
\end{aligned} \tag{4.12}$$

Accordingly, equations (4.4)–(4.6) are reformulated, but they maintain exactly the same format, with the dimensional quantities replaced by the corresponding nondimensionalized counterparts: that is

$$\begin{aligned}
\{R^{*}\} &= E_r^{-1} r_r^{1-s}\{R\}, \\
\{u^{*}\} &= r_r^{-1}\{u\}, \\
\{u^{(i)*}\} &= (E_r r_r^{s-1})^{-N_i}\{u^{(i)}\}.
\end{aligned} \tag{4.13}$$

In order to incorporate the proposed parametric nondimensionalization scheme into the SBFEM calculation, a group of reference variables need to be specified, so that all relevant quantities involved in the calculation are of similar magnitude. Precision has to be considered at various intermediate stages, such as the real Schur decomposition of the Hamiltonian matrix $[Z]$ and the general eigenvalue decomposition of $[E^0]$ and $[M^0]$. In addition, the stiffness matrices $[K]$ and $[K_{\infty}]$, the mass matrix $[M]$, the damping matrices $[C]$ and $[C_{\infty}]$, and the auxiliary matrices $[Y_1^{(i)}]$ and $[Y_0^{(i)}]$ $(i = 1, 2, 3 \ldots)$ associated with the continued fraction are required, to satisfy the corresponding algebraic equations.

Equations (4.7), (4.9)–(4.10) and (4.12)–(4.13) illustrate how matrices are nondimensionalized with respect to the reference variables. They are not explicitly formulated in the solution procedure. Calculated results are dimensionless and require subsequent interpretation in order to be applied to engineering problems. For example, a variable with dimension L should be multiplied by the reference length r_r to obtain the corresponding dimensional value. The following examples will detail these procedures.

4.3. Numerical examples

4.3.1 Static analysis The cylindrical pile in Section 3.3 is reconsidered with four sets of reference variables, as shown in Table 1, to demonstrate SBFEM nondimensionalization. Taking into account the magnitude of the input parameters, four values of E_r are selected as 1 Pa, 1×10^3 Pa, 1×10^7 Pa and 2.8×10^{10} Pa to nondimensionalise the Young's modulus E and the external pressure p, both of which have dimensions $ML^{-1}T^{-2}$. The reference length r_r equals 1 m, as the same SBFEM model is used for the four cases and the dimension of the model is identical to the physical prototype of the pile. The mass density is irrelevant in this example and therefore is not discussed. For each of the four cases, the maximum difference $\Delta M_{\max}$

https://doi.org/10.1017/S1446181115000255 Published online by Cambridge University Press

Table 1. Numerical performance of SBFEM using a static analysis.

Parameters \ Set number	1	2	3	4
E_r (Pa)	1	1×10^3	1×10^7	2.8×10^{10}
r_r (m)	1	1	1	1
$\Delta M_{\max}$	4×10^{10}	4×10^7	4×10^3	138.74
κ	2×10^{24}	8×10^{16}	8×10^8	2×10^5
Res_1	0.1345	1×10^{-4}	3×10^{-8}	7×10^{-11}
Res_2	9×10^{21}	1×10^9	0.0011	9×10^{-12}
u_x (mm)	4.431×10^3	11.507	8.0357	8.0357
u_y (mm)	1.4205×10^4	5.744	4.625×10^{-8}	1.394×10^{-8}
u_z (mm)	7.178×10^4	51.534	52.358	52.358

in the magnitude of the entries of the Hamiltonian matrix and the condition number κ of the Hamiltonian matrix, as well as the norms of the two residual matrices Res_1 and Res_2, are examined. The displacement components u_x, u_y and u_z of point A are transferred into the corresponding dimensional values and are listed in Table 1.

Evaluating the four indices, $\Delta M_{\max x}$, κ, Res_1 and Res_2, we find that the numerical performance of the SBFEM calculation improves as the reference parameter E_r gradually increases. The maximum magnitude difference among the entries of the matrix $[Z]$ decreases from a magnitude of 10^{10} to 10^2, and its condition number decreases from 10^{24} to 10^5. Consequently, the norms of the two residual matrices are found to converge to zero when E_r reaches 2.8×10^{10} Pa. The readings of the displacement components also indicate a trustworthy calculation, when appropriate reference variables are employed. Note that the reference parameters should be defined in such a way that all variables involved in the matrix calculation hold similar magnitude regardless of their dimensions. For the present case, a combination of $E_r = 2.8 \times 10^{10}$ Pa and $r_r = 1$ m generates a magnitude of one for both the length L and pressure $ML^{-1}T^{-2}$.

4.3.2 Modal analysis The case in Section 4.3.1 examines how the accuracy of SBFEM results is affected by the magnitude of input parameters in statical analysis, and thus highlights the necessity of parametric nondimensionalization in the SBFEM calculation. The modal analysis presented in this section and the transient analysis in the next section will examine the performance of the dimensionless SBFEM calculation in elasto-dynamics. The L-shaped panel of Song [18] is re-examined here with the same geometric configuration. Young's modulus E and the mass density ρ are assigned the values 2.8×10^{10} Pa and 2400 kg m^{-3}, respectively, with a Poisson's ratio 1/3.

A sketch of the L-shaped panel is reproduced in Figure 9(a), illustrating the geometric configuration ($b = 1$ m) and the boundary conditions; line EF is fully constrained in both x- and y-directions and AB is fixed only in the x-direction.

https://doi.org/10.1017/S1446181115000255 Published online by Cambridge University Press

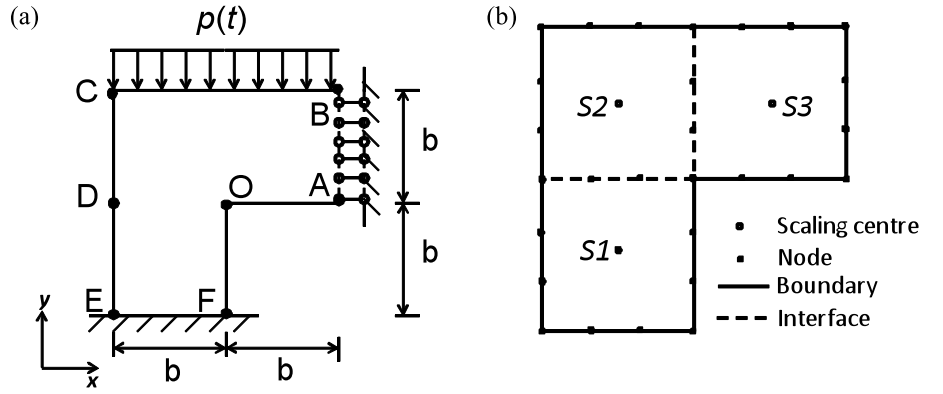

FIGURE 9. *L*-shaped panel: (a) geometry of the panel and its boundary conditions (reproduced from [17]) (b) the SBFEM mode.

In the SBFEM model shown in Figure 9(b), the *L*-shaped panel is divided into three subdomains with the scaling centres located at the geometric centre of each subdomain. Therefore, all the boundaries as well as the two interfaces between the subdomains are discretized. This analysis can also be carried out by treating the *L*-shaped panel as a single domain and locating the scaling centre at the point O, and thus only those lines other than OA and OF need to be discretized. Three-node quadratic elements are used for the boundary discretization, which results in 196 degrees of freedom for the problem. The continued-fraction technique is employed and an order of six is used when formulating the global stiffness and mass matrices. Here the reference parameters are $r_r = 1$ m, $E_r = 2.8 \times 10^{10}$ Pa and $\rho_r = 2400$ kg m^{-3}.

The first 110-order dimensionless natural frequencies calculated from SBFEM are plotted in Figure 10(a). From equation (4.8), we obtain the dimensional natural frequencies

$$\omega = \frac{\sqrt{E_r/\rho_r}}{r_r}\omega^*$$

and compare this with the result of an equivalent FEM modal analysis in Figure 10(b). The two curves agree extremely well. The same analysis using dimensional parameters in the SBFEM model is also attempted, but it fails due to the error accumulation during the calculation process, which renders the subsequent results meaningless.

4.3.3 Transient analysis Here, we use the *L*-shaped panel to illustrate the effect of a parametric nondimensionalization on the transient analysis. A force condition, similar to that described by Song [18], is specified and is uniformly distributed along line BC (Figure 9(a)) with the magnitude varying with respect to time, as shown in Figure 11(a). The values of p_{peak}, t_{total}, t_{peak} and t_{zero} are given in Table 2, in which dimensional and nondimensional parameters are listed.

https://doi.org/10.1017/S1446181115000255 Published online by Cambridge University Press

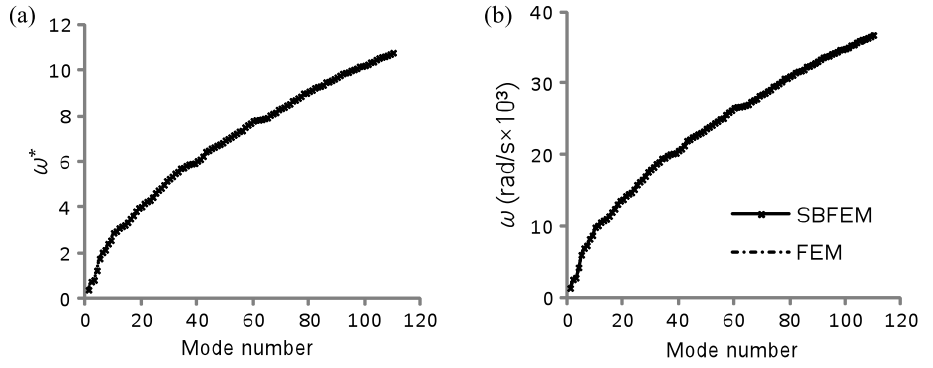

FIGURE 10. Natural frequency of the *L*-shaped panel: (a) dimensionless natural frequency from SBFEM model (b) comparison of dimensional natural frequencies between FEM and SBFEM results.

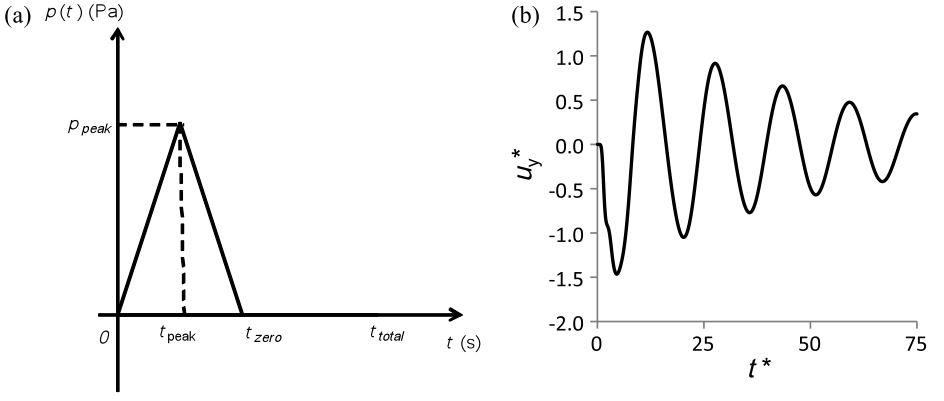

FIGURE 11. SBFEM transient analysis of an *L*-shaped panel: (a) pressure variation with respect to time (b) dimensionless displacement in the *y*-direction of point *A*.

TABLE 2. Parameters of the transient analysis of an *L*-shaped panel.

		Dimensional		Nondimensional
Material parameters	E (Pa)	2.8×10^{10}	E^*	1
	ρ (kg m^{-3})	2400	ρ^*	1
Temporal variables	t_{total} (s)	0.022	t^*_{total}	75
	t_{peak} (s)	1.4639×10^{-4}	t^*_{peak}	0.5
	t_{zero} (s)	2.9277×10^{-4}	t^*_{zero}	1
	Δt (s)	7.3193×10^{-6}	Δt^*	0.025
Natural circular frequencies	ω_1 (rad s^{-1})	1371.682	ω^*_1	0.4032
	ω_2 (rad s^{-1})	2819.265	ω^*_2	0.8259
External pressure	p_{peak} (Pa)	2.8×10^7	p^*_{peak}	1×10^{-3}

https://doi.org/10.1017/S1446181115000255 Published online by Cambridge University Press

Table 3. Comparison of magnitudes of entries before and after nondimensionalization.

Matrices	Before nondimensionalization			After nondimensionalization		
	x	y	z	x	y	z
$[K_\infty]$	4.52×10^{10}	4.52×10^{10}	6.21×10^{10}	4.52×10^{0}	4.52×10^{0}	6.21×10^{0}
$[Y_0^{(1)}]$	2.15×10^{-7}	2.15×10^{-7}	2.54×10^{-6}	2.15×10^{3}	2.15×10^{3}	2.54×10^{4}
$[Y_0^{(2)}]$	7.71×10^{10}	7.71×10^{10}	7.22×10^{11}	7.71×10^{0}	7.71×10^{0}	7.22×10^{1}
$[Y_0^{(3)}]$	-1.51×10^{-4}	-1.51×10^{-4}	-5.19×10^{-3}	-1.51×10^{6}	-1.51×10^{6}	-5.19×10^{7}
$[Y_0^{(4)}]$	-2.93×10^{14}	-2.75×10^{14}	-5.92×10^{15}	-1.31×10^{4}	-1.35×10^{4}	-2.92×10^{4}
$[Y_0^{(5)}]$	1.55×10^{-3}	-1.24×10^{-3}	2.06×10^{-1}	3.03×10^{9}	1.14×10^{9}	4.82×10^{9}
$[Y_0^{(6)}]$	-4.91×10^{17}	-4.06×10^{17}	-2.87×10^{17}	2.79×10^{7}	9.48×10^{5}	-1.99×10^{6}
$[Y_0^{(7)}]$	3.06×10^{-5}	-1.26×10^{-5}	2.73×10^{-4}	5.02×10^{8}	6.25×10^{8}	-1.42×10^{10}
$[Y_0^{(8)}]$	-6.98×10^{16}	2.02×10^{17}	-5.57×10^{16}	7.62×10^{3}	7.04×10^{3}	5.17×10^{4}

The SBFEM analysis adopts the same discretization model (see Figure 9(b)), and the reference material properties E_r and ρ_r are chosen as 2.8×10^{10} Pa and 2400 kg m^{-3}, respectively. Using Newmark's integral technique with $\alpha = 0.25$ and $\delta = 0.5$ [4], all the temporal variables associated with the time integration are nondimensionalized by equation (4.11). The damping effect of Rayleigh material is taken into account with a material damping ratio of 0.05, assuming that the L-shaped panel is made of concrete. From the modal analysis in Section 4.3.2, $\omega_1 = 1371.682$ rad s^{-1} and $\omega_2 = 2819.265$ rad s^{-1}, are selected, corresponding to two orthogonal modal shapes. However, their dimensionless counterparts are used for the formulation of the damping matrix. The magnitude of the external pressure at any time step is nondimensionalized according to the Young's modulus.

The dimensionless displacement history of point A (see Figure 9(a)) in the y-direction is shown in Figure 11(b). With reference length $r_r = 1$ m, the dimensional displacement should hold the same amplitude as u_y^*, whereas the time variable should be calculated by reformulating equation (4.11) in terms of t to obtain its dimensional counterpart.

An equivalent FEM analysis is also carried out for comparison purposes. We observe excellent agreement between FEM and SBFEM results in Figure 12, which compares the displacement in the x- and y-directions of point O and the displacement histories in the y-direction of points C and D (Figure 9(a)) from both FEM and SBFEM calculations. Use of original parameters in the SBFEM analysis does not produce any realistic result.

4.3.4 Wave propagation in unbounded domains Revisiting the example of elastic wave propagation in an unbounded domain in Section 4.2, we observe that the application of the nondimensionalization process with reference parameters $r_r = 1$ m, $G_r = 1 \times 10^{10}$ Pa and $\rho_r = 2500$ kg m^{-3} significantly reduces the degree of difference between the magnitudes of matrix entries. As shown in Table 3, for a continued-fraction order M_{cf} up to eight, the variation in the magnitude of matrix elements is between 1×10^0 and 1×10^{10}, as opposed to 1×10^{-7} and 1×10^{17} when using dimensional parameters. Therefore, using equation (4.6), the difference in the magnitude of the largest and the smallest elements in $[A]$ can be reduced from 10^{24} to 10^{10}. The component of the dynamic stiffness matrix in the z-direction of the unbounded domain calculated at specified frequencies before and after applying the nondimensionalization scheme is compared in Figure 13. Note that, using dimensional parameters, the dynamic stiffness matrix becomes substantially different from that using dimensionless parameters. Due to the unfavourable matrix properties, calculations using dimensional parameters potentially lead to erroneous results or even terminate the calculation in the process of matrix manipulations. By improving the properties of the coefficient matrices, the nondimensionalization scheme undoubtedly enhances the credibility of SBFEM calculations.

https://doi.org/10.1017/S1446181115000255 Published online by Cambridge University Press

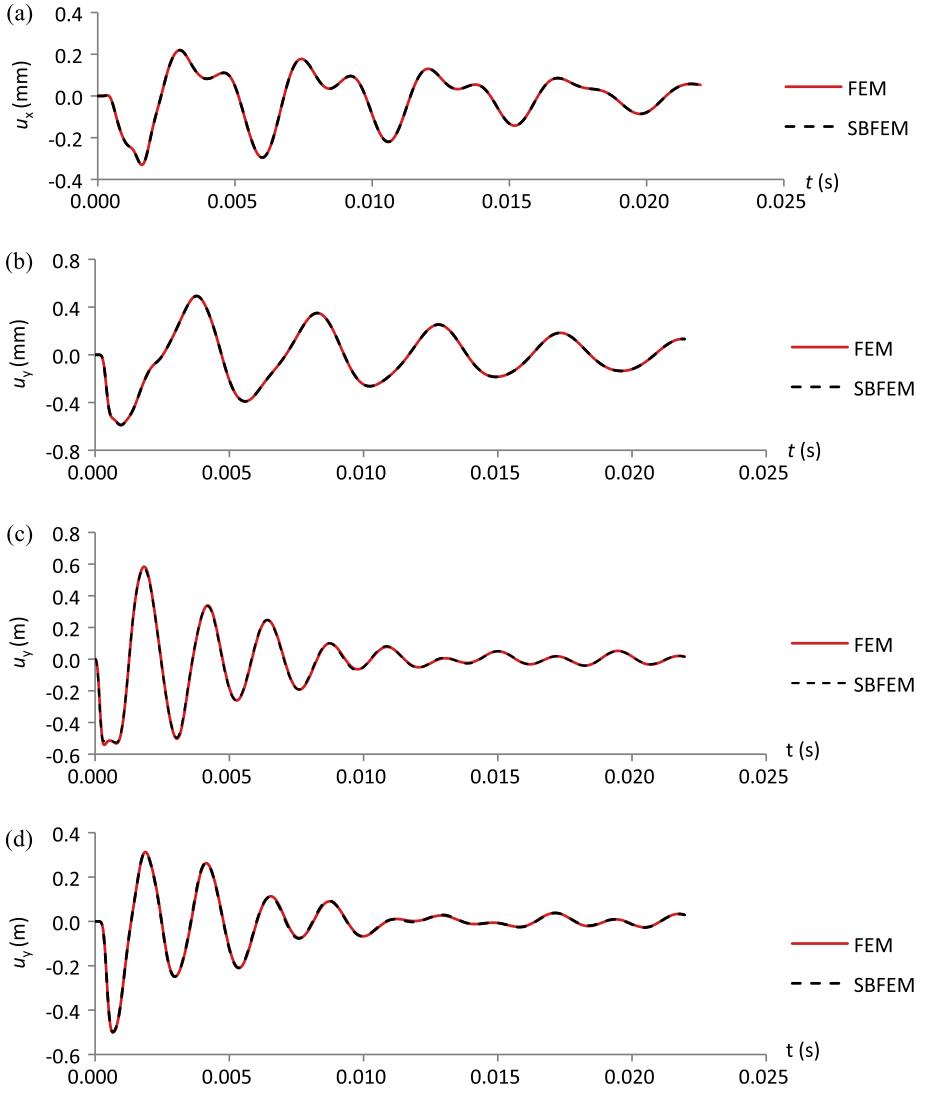

FIGURE 12. Comparison of displacement history between SBFEM and FEM models: (a) in the x-direction of point O, (b) in the y-direction of point O, (c) in the y-direction of point C and (d) in the y-direction of point D.

5. Conclusion

The intense matrix calculations involved in SBFEM result in numerical instability when solving engineering problems. Therefore, in this study, we focus on the numerical performance of SBFEM which has not been systematically addressed in the literature. There are two aspects of this discussion, namely, the matrix manipulation technique and the matrix properties. The eigenvalue decomposition

https://doi.org/10.1017/S1446181115000255 Published online by Cambridge University Press

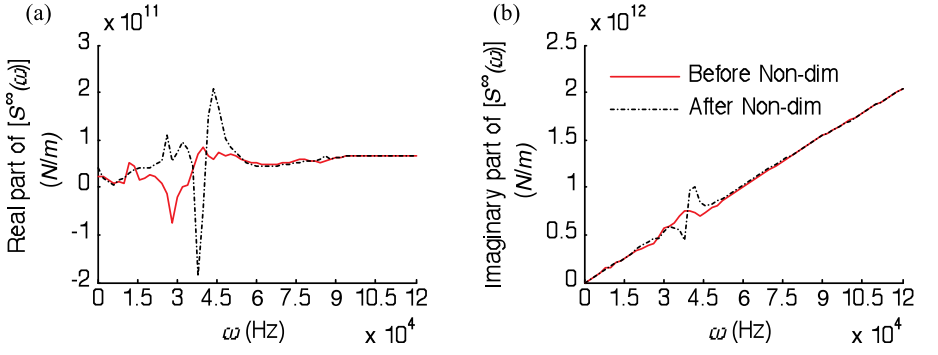

FIGURE 13. Comparison of the vertical dynamic stiffness coefficient before and after applying the nondimensionalization scheme of an elastic wave propagation problem in an unbounded domain: (a) real part of $[S^8(\omega)]$ *vs* frequency (b) imaginary part of $[S^8(\omega)]$ *vs* frequency. (Bold line for "before" and dashed line for "after" nondimensionalization.)

of the Hamiltonian matrix leads to the underlying multiple eigenvalues associated with possible logarithmic terms in the solution. The real Schur decomposition can be adapted as an alternative, since it circumvents this problem and provides more stable and accurate solutions. Furthermore, no manipulation of complex numbers is required in the eigenvalue decomposition. A case study of a cylindrical pile subjected to uniformly distributed pressure along the circumferential direction shows a better performance by the real Schur decomposition compared with the eigenvalue decomposition.

On the other hand, since SBFEM relies on intense matrix computations, the properties of all relevant matrices are important for establishing the stability and accuracy of the results. Therefore, we propose that a group of reference variables be predefined so as to nondimensionalize the input parameters, such as the geometric dimension, material properties and temporal variables, before performing the calculation by SBFEM. All relevant matrices thus present favourable properties to ensure the correctness of the calculations. Numerical examples with respect to elasto-statics, modal and transient analyses, and the wave propagation problem in an unbounded domain formulated using the continued-fraction technique, show enhanced performance of SBFEM after applying the proposed nondimensionalization scheme. This study clarifies the reasons for potential numerical instability and inaccuracy of SBFEM, and corresponding solution schemes are proposed to rectify these issues. Overall, the study is expected to guarantee a reliable implementation of SBFEM when solving engineering problems.

References

[1] M. H. Bazyar and C. M. Song, "A continued-fraction-based high-order transmitting boundary for wave propagation in unbounded domains of arbitrary geometry", *Int. J. Numer. Meth. Eng.* **74** (2008) 209–237; doi:10.1002/nme.2147.

https://doi.org/10.1017/S1446181115000255 Published online by Cambridge University Press

[2] C. Birk, S. Prempramote and C. Song, "An improved continued-fraction-based high-order transmitting boundary for time-domain analyses in unbounded domains", *Int. J. Numer. Meth. Eng.* **89** (2012) 269–298; doi:10.1002/nme.3238.

[3] D. H. Chen, "Logarithmic singular stress field in a semi-infinite plate consisting of two edge-bonded wedges subjected to surface tractions", *Int. J. Fract.* **75** (1996) 357–378; doi:10.1007/bf00019615.

[4] R. W. Clough and J. Penzien, *Dynamics of structures* (McGraw-Hill, New York, 1975).

[5] A. J. Deeks and J. P. Wolf, "Semi-analytical elastostatic analysis of unbounded two-dimensional domains", *Int. J. Numer. Anal. Methods Geomech.* **26** (2002) 1031–1057; doi:10.1002/Nag.232.

[6] A. J. Deeks and J. P. Wolf, "A virtual work derivation of the scaled boundary finite-element method for elastostatics", *Comput. Mech.* **28** (2002) 489–504; doi:10.1007/s00466-002-0314-2.

[7] A. J. Deeks and J. P. Wolf, "Semi-analytical solution of Laplace's equation in non-equilibrating unbounded problems", *Comput. Struct.* **81** (2003) 1525–1537; doi:10.1016/S0045-7949(03)00144-5.

[8] K. S. Gadi, P. F. Joseph, N. S. Zhang and A. C. Kaya, "Thermally induced logarithmic stress singularities in a composite wedge and other anomalies", *Eng. Fract. Mech.* **65** (2000) 645–664; doi:10.1016/S0013-7944(99)00145-9.

[9] D. Goldberg, "What every computer scientist should know about floating-point arithmetic", *ACM Comput. Surverys* **23** (1991) 5–48; doi:10.1145/103162.103163.

[10] B. N. Li, Extending the scaled boundary finite element method to wave diffraction problems, Ph.D. Thesis, The University of Western Australia, 2007.

[11] B. N. Li, L. Cheng, A. J. Deeks and M. Zhao, "A semi-analytical solution method for two-dimensional Helmholtz equation", *Appl. Ocean Res.* **28** (2006) 193–207; doi:10.1016/j.apor.2006.06.003.

[12] M. Li, H. Song, H. Guan and H. Zhang, "Schur decomposition in the scaled boundary finite element method in elastostatics", *Proc. of the 9th World Congress on Comp. Mech. (WCCM) and 4th Asia-Pacific Congress on Comp. Mech. 2010 (APCOM), Minisymposia – The Scaled Boundary Finite Element Method* (Sydney, Australia, 2010).

[13] J. Liu, G. Lin, W. FM and J. Li, "The scaled boundary finite element method applied to Electromagnetic field problems", *9th World Congress on Comp. Mech. and 4th Asian Pacific Congress on Comp. Mech.* (Sydney, Australia, 2010).

[14] C. Paige and C. Vanloan, "A Schur Decomposition for Hamiltonian Matrices", *Linear Algebra Appl.* **41** (1981) 11–32; doi:10.1016/0024-3795(81)90086-0.

[15] G. B. Sinclair, "Logarithmic stress singularities resulting from various boundary conditions in angular corners of plates in extension", *J. Appl. Mech.* **66** (1999) 556–560; doi:110.1115/1.2791085.

[16] G. B. Sinclair, "Logarithmic stress singularities resulting from various boundary conditions in angular corners of plates under bending", *J. Appl. Mech.* **67** (2000) 219–223; doi:10.1115/1.321174.

[17] C. M. Song, "A matrix function solution for the scaled boundary finite-element equation in statics", *Comput. Methods Appl. Math.* **193** (2004) 2325–2356; doi:10.1016/j.cma.2004.01.017.

[18] C. M. Song, "The scaled boundary finite element method in structural dynamics", *Int. J. Numer. Meth. Eng.* **77** (2009) 1139–1171; doi:10.1002/Nme.2454.

[19] C. M. Song and J. P. Wolf, "Consistent infinitesimal finite-element cell method for diffusion equation in unbounded domain", *Comput. Methods Appl. Math.* **132** (1996) 319–334; doi:10.1016/0045-7825(96)01029-8.

[20] C. M. Song and J. P. Wolf, "The scaled boundary finite-element method – alias consistent infinitesimal finite-element cell method – for elastodynamics", *Comput. Methods Appl. Math.* **147** (1997) 329–355; doi:10.1016/S0045-7825(97)00021-2.

[21] C. M. Song and J. P. Wolf, "The scaled boundary finite-element method: analytical solution in frequency domain", *Comput. Methods Appl. Math.* **164** (1998) 249–264; doi:10.1016/S0045-7825(98)00058-9.

[22] C. M. Song and J. P. Wolf, "The scaled boundary finite-element method – a primer: solution procedures", *Comput. Struct.* **78** (2000) 211–225; doi:10.1016/S0045-7825(98)00058-9.

[23] H. Song, L. B. Tao and S. Chakrabarti, "Modelling of water wave interaction with multiple cylinders of arbitrary shape", *J. Comput. Phys.* **229** (2010) 1498–1513; doi:10.1016/j.jcp.2009.10.041.

[24] L. B. Tao, H. Song and S. Chakrabarti, "Scaled boundary FEM solution of short-crested wave diffraction by a vertical cylinder", *Comput. Methods Appl. Math.* **197** (2007) 232–242; doi:10.1016/j.cma.2007.07.025.

[25] J. P. Wolf and C. M. Song, *Finite-element modelling of unbounded media* (Wiley, Chichester, 1996).

[26] J. P. Wolf and C. M. Song, "The scaled boundary finite-element method – a primer: derivations", *Comput. Struct.* **78** (2000) 191–210; doi:10.1016/S0045-7949(00)00099-7.

[27] J. P. Wolf and C. M. Song, "The scaled boundary finite-element method – a fundamental solution-less boundary-element method", *Comput. Methods Appl. Math.* **190** (2001) 5551–5568; doi:10.1016/S0045-7825(01)00183-9.

[28] Z. J. Yang, "Fully automatic modelling of mixed-mode crack propagation using scaled boundary finite element method", *Eng. Fract. Mech.* **73** (2006) 1711–1731; doi:10.1016/j.engfracmech.2006.02.004.

[29] Z. J. Yang and A. J. Deeks, "Fully-automatic modelling of cohesive crack growth using a finite element-scaled boundary finite element coupled method", *Eng. Fract. Mech.* **74** (2007) 2547–2573; doi:10.1016/j.engfracmech.2006.12.001.

[30] Z. J. Yang and A. J. Deeks, "Modelling cohesive crack growth using a two-step finite element-scaled boundary finite element coupled method", *Int. J. Fract.* **143** (2007) 333–354; doi:10.1007/s10704-007-9065-6.